Journal of Energy Storage 152 (2026) 120760

Contents lists available at ScienceDirect

Journal of Energy Storage

journal homepage: www.elsevier.com/locate/est

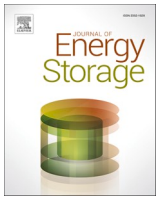

Research papers

Influence of the physical properties of electrolytes on the behavior of all-vanadium redox flow batteries

Álvaro Ibáñez [a,*], Manuel Montiel [a,b,**], Andrés Tejero [a], Ignacio Ortiz de Landazuri [a], Antonio Lozano [a], Jorge Barroso [c], Félix Barreras [a,*]

[a] Instituto de Carboquímica (ICB), Consejo Superior de Investigaciones Científicas (CSIC), C/Miguel Luesma Castán, 4, 50018, Zaragoza, Spain
[b] Fundación Agencia Aragonesa para la Investigación y el Desarrollo (ARAID), Av. de Ranillas 1-D, 50018, Zaragoza, Spain
[c] Laboratorio de Ingeniería de Fluidos y Energía (LIFEn) - Instituto Universitario de Investigación en Ingeniería de Aragón (I3A), Universidad de Zaragoza, C/María de Luna 3, 50018, Zaragoza, Spain

ARTICLE INFO

Dataset link: Influence of the physical properties of electrolytes on the behavior of all-vanadium redox flow batteries (Original data)

Keywords:
Vanadium redox flow batteries
Electrolyte
Density
Viscosity
State of charge
Flow rate

ABSTRACT

Electrolyte flow rate has a large impact on the overall efficiency and energy storage capacity of all-vanadium redox flow batteries. This work focuses on the detailed determination of density and viscosity of vanadium electrolytes as a function of temperature and state of charge, as well as their influence on the actual electrolyte flow rate. Negative and positive electrolytes present different density and viscosity values and they also evolve differently, the divergence being especially significant in the dynamic viscosity. Mathematical correlations of experimental data are provided, and the influence of these properties on both hydraulic and electrochemical performance of the device is also discussed. An ad hoc experimental facility was manufactured where a 200 W battery was tested to assess the relevance of the different hydraulic conditions on the pressure drop and efficiency. A notable decrease in the total duration of the 5 charge/discharge cycles when the circulating flow rates were progressively reduced was observed. The average efficiency of the battery varied from 73.9% to 67.5% when decreasing the flow rate levels. In addition, a low-cost computational model was developed to estimate the circulating flow rate of each electrolyte and to discriminate the contribution of the specific pressure loss from the different components of the facility for a given operating condition.

1. Introduction

The global reliance of energy production on fossil fuels has led to critical issues related to energy security and environmental pollution, intensifying global climate concerns. Consequently, terms like “decarbonization” and “ecological transition” are now widely adopted by both experts and ordinary people. Therefore, many regions, including all European Countries, have proposed a shift towards energy models that prioritize renewable sources. As an example, renewable energy production in Spain has been significantly increased from 94 TW·h in 2015 to 149 TW·h in 2024 [1]. However, the inherent intermittency and unpredictability of these environmentally friendly sources, due to their dependence on weather conditions, result in low-quality electrical signal output and grid instability. To address these challenges, renewable-based electrical grids must incorporate large-scale energy storage systems (ESS), capable of accumulating and releasing electricity as required, thereby enhancing energy quality, reliability, and balancing supply with demand [2].

Even though numerous ESS technologies exist at different stages of development (mechanical, chemical, electrical, or thermal among others [3]), a variety of rechargeable batteries have been explored due to their modularity, high energy efficiency and connection versatility. The widespread adoption of batteries for large-scale ESS has been significantly influenced by their capital costs. This is exemplified by the recent reduction in the price of lithium-ion batteries (LIB), which has enabled their broader market penetration [4]. Despite their advantages, the widespread LIB deployment for ESS faces significant challenges in the coming years. Firstly, the high demand of lithium by the electric vehicle sector, increases the concern about resource availability and supply chain stability for large-scale stationary systems. Secondly, large-scale LIB systems can present inherent safety issues, such as thermal runaway and fire risks, which become more pronounced with increasing

* Corresponding authors.
** Correspondence to: M. Montiel, Fundación Agencia Aragonesa para la Investigación y el Desarrollo (ARAID), Av. de Ranillas 1-D, 50018, Zaragoza, Spain.
E-mail addresses: ibz.alvaro@gmail.com (Á. Ibáñez), manuel.montiel@csic.es (M. Montiel), felix.barreras@csic.es (F. Barreras).

https://doi.org/10.1016/j.est.2026.120760
Received 5 September 2025; Received in revised form 26 December 2025; Accepted 23 January 2026
Available online 30 January 2026

system size. These factors underscore the need for finding alternative storage technologies for these applications.

In this sense, redox flow batteries (RFBs) have gained considerable attention as large-scale ESS due to their environmental friendliness and flexible design, notably because power and capacity are decoupled. In addition, RFBs possess attractive features, including a long operational lifetime, high safety, and acceptable round-trip efficiency. In recent years, the all-vanadium redox flow batteries (VRFBs) proposed by Skyllas-Kazacos et al. [5] have undergone significant development. Several demonstration projects, spanning from tens of kW to MW, have been successfully implemented, thereby asserting their technological feasibility for large-scale applications [6–8]. Unlike traditional batteries, the energy stored in VRFB depends on the volume of electrolytes accumulated in external tanks. The electrolytes, typically liquid solutions of active materials, are continuously pumped from the reservoirs to the electrochemical cells (stacks) during charge and discharge processes, then returning to the tanks. The energy capacity of a VRFB can be easily enhanced by increasing the electrolyte volume available in the reservoirs. This technology eases the dimensioning and facilitates the adaptability to industrial-scale conditions without significant additional costs, since the tanks can be manufactured to the desired size. This implies that as the energy capacity of a VRFB increases, the price per kilowatt-hour decreases [6,9].

In the existing literature on VRFBs, detailed studies have been conducted on key materials and components, such as membranes or electrodes. However, despite the critical relevance of the flow conditions and the physical properties of vanadium electrolytes within the stacks and pipe network to the battery performance and operation, less research has been focused on this area. For example, density variations in the fluid circulating through the battery can result in the formation of zones with unreacted electrolyte species within the tanks resulting in subsequent stratification, which may decrease the battery capacity [10]. Several research teams have conducted density measurements for negative [11], positive [12,13] or both electrolytes [14–16], studying their dependence on vanadium concentration, sulfate concentration, temperature, and state of charge (SOC). On the other hand, the electrolyte dynamic viscosity plays a relevant role on the overall VRFB energy efficiency, due to increased power consumption associated to electrolyte pumping (especially when circulating through the electrode porous medium). Moreover, viscosity changes are mainly influenced by the electrolyte temperature and active species concentration, affecting ion mass transport and, consequently, the overall electrochemical performance [11,17–19].

In numerous VRFB models, it is usual to treat parameters such as density and viscosity as constant and equal for both positive and negative electrolytes. While this simplification may reduce programming complexity, it can lead to inaccuracies since this assumption does not fully reflect reality: the physical properties of actual electrolytes differ and change during VRFB operation. This is particularly critical for the device control and to optimize the battery energy efficiency. Therefore, accounting for viscosity and density variations as a function of SOC and temperature would enable the optimization of flow rates and pumping power, thereby minimizing not only energy consumption but also vanadium crossover resulting from pressure differences between half-cells.

The objective of this work is to analyze the influence of electrolyte physical properties and flow rate on the performance of a VRFB. To this end, a detailed characterization of the density and dynamic viscosity of vanadium electrolytes as a function of their temperature and SOC was performed. Moving beyond fundamental property characterization, this study evaluates the direct impact of these variations on the hydraulic and electrochemical performance of a 200 W stack. To facilitate this analysis on actual batteries, a VRFB testing facility was designed and manufactured. Furthermore, its hydraulic dynamics was modeled to enable the quantification of different contributions to total pressure losses and the prediction of the electrolyte flow rate, effectively bridging the gap between electrolyte physical behavior and operational system efficiency.

2. Technology principle

Briefly, a VRFB is a type of rechargeable battery that uses dissolved vanadium ions in different oxidation states to store energy. It consists of an assembly of cells, each half-cell separated by an ion exchange membrane. The typical electrolyte in VRFBs is an aqueous solution of 1–2 M vanadium ions with a supporting electrolyte, usually 1–3 M sulfuric acid. Some other additives are used to enhance its thermal stability and other physicochemical properties. Vanadium exists in four oxidation states: VO^{2+} [V(IV), blue], VO_2^+ [V(V), yellow], V^{2+} [V(II), violet], and V^{3+} [V(III), green]. As depicted in Fig. 1, the positive electrolyte (posolyte) utilizes the VO^{2+}/VO_2^+ redox couple, and the negative one (negolyte) uses the V^{2+}/V^{3+}. The charge and discharge of the entire device involve the oxidation and reduction faradic processes of the different vanadium ions.

During the discharge process, in the negative half-cell, V(II) ions are oxidized to V(III) releasing an electron for electrical conduction:

$$V^{2+} \leftrightarrow V^{3+} + e^- \quad \left(E^0 = -0.255\ V\ vs.\ SHE\right) \tag{1}$$

Conversely, in the positive half-cell, V(V) ions are reduced to V(IV), gaining the electron released from the negative half-cell:

$$VO_2^+ + e^- + 2H^+ \leftrightarrow VO^{2+} + H_2O \quad \left(E^0 = 1.004\ V\ vs.\ SHE\right) \tag{2}$$

Thus, the overall reaction is

$$VO_2^+ + V^{2+} + 2H^+ \leftrightarrow VO^{2+} + V^{3+} + H_2O \quad \left(E^0 = 1.259\ V\ vs.\ SHE\right) \tag{3}$$

During the charge and discharge processes, hydrogen ions (H^+) are consumed or produced and, consequently, the pH of the positive and the negative electrolytes change over time. To maintain the balance of charge within the half-cells, H^+ transit occurs between the negative and positive half-cells through the polymeric membrane.

3. Experimental procedure

3.1. Electrolyte characterization and vanadium species generation

According to the supplier specifications (HydraRedox Iberia), the commercial electrolyte characterized in this study is a solution of 2 M sulfuric acid (H_2SO_4), 0.05 M phosphoric acid (H_3PO_4), and a vanadium concentration between 1.65 M and 1.75 M, consisting of a mixture of V(III) and V(IV) in a 50%-50% proportion. The actual vanadium concentration and species distribution were determined via potentiometric titrations. In this technique, the target solution potential with respect to a reference electrode (Ag/AgCl) is continuously monitored. Subsequently, a solution 0.033 M of potassium permanganate $KMnO_4$ (ITW Reagents) was gradually added until a sharp change in voltage was recorded. Prior to this, the potassium permanganate was standardized using a 0.167 M solution of sodium oxalate $Na_2C_2O_4$ (Aldrich Chemical Company) as the primary standard. During the electrolyte titration, two abrupt voltage changes were observed: the first one indicates the oxidation of V(III) to V(IV), and the second one the oxidation of V(IV) to V(V), this one occurring after all V(III) was oxidized. To enhance the results reliability, three titrations were performed on 1:10 electrolyte solutions. An aqueous H_2SO_4 2 M solution was used as the supporting electrolyte to increase the medium conductivity. After these experiments, the vanadium concentration was determined to be 1.70 M, with a distribution of 54.2% V(III) and 45.8% V(IV).

Following the assessment and composition determination of the commercial electrolyte, sufficient volumes of each vanadium species were produced by repeated charge-discharge cycles using a 5-cell VRFB stack with an electrode area of 60 cm^2. For charging, a constant voltage of 8 V (1.6 V/cell), an initial current of 5 A (83.3 mA/cm^2), and final current below 0.24 A (4 mA/cm^2) were applied. On the contrary, for

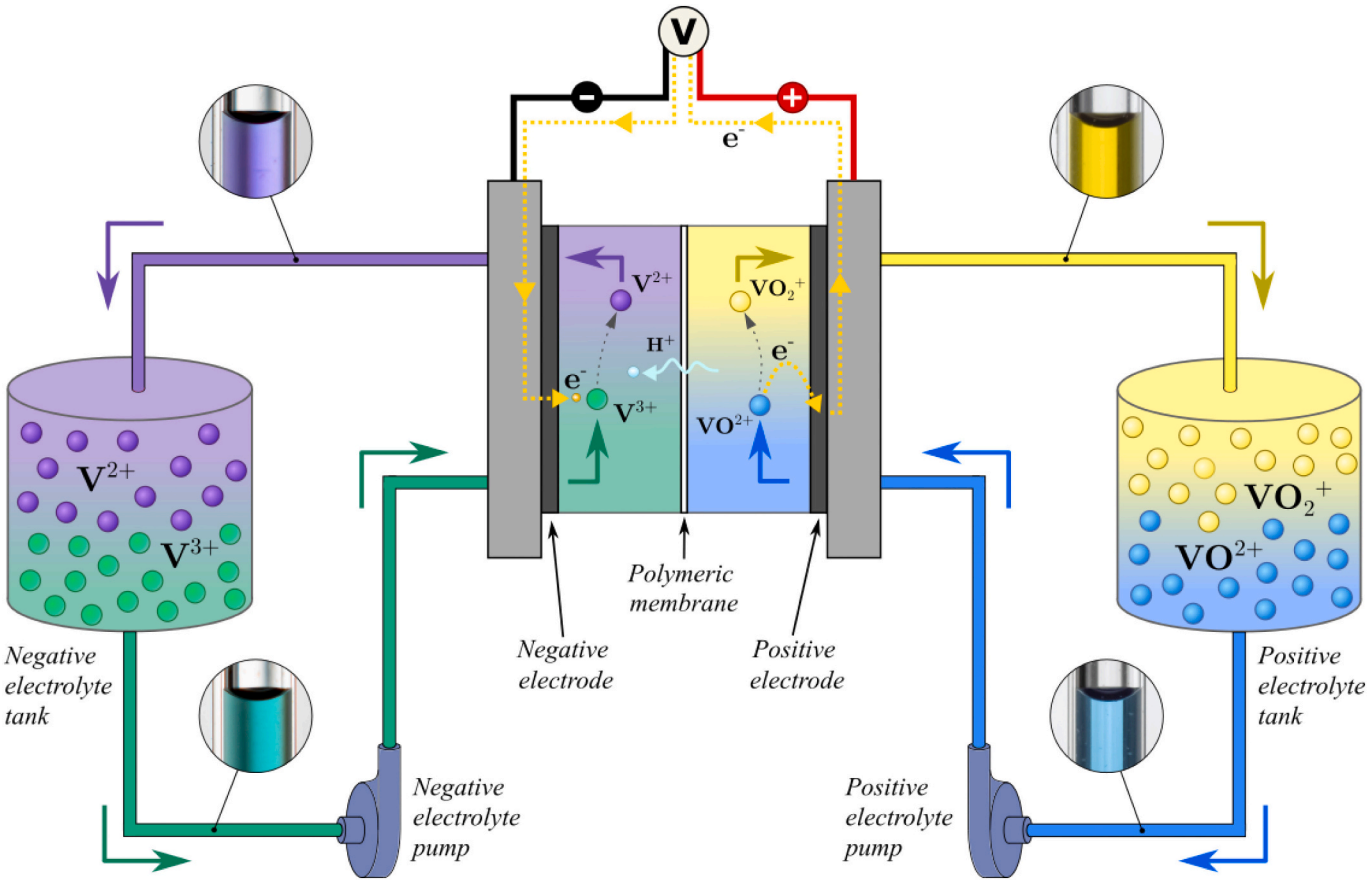

Fig. 1. Schematic representation of the charging process of a VRFB cell.

discharging, a constant current of 6 A (100 mA/cm^2) was demanded until the voltage dropped below 0.2 V (40 mV/cell). To ensure species purity, V(V) and V(IV) were prepared with excess negolyte, while V(III) and V(II) were prepared with excess posolyte.

After the potentiometric experiments, the commercial vanadium electrolyte underwent further characterization via ultraviolet-visible spectroscopy (UV–Vis). Each of the generated volumes was analyzed to ensure their purity [20]. Fig. 2 (top) shows the measured spectra for wavelengths ranging between 300 nm and 1100 nm, which are consistent with literature reports. Afterwards, samples for both electrolytes were prepared from the pure species at various known dilution levels to measure their spectra. Based on these results and applying Beer-Lambert's law, a code was developed to calculate the composition and concentration of a posolyte or negolyte sample from its spectrum.

3.2. Density measurements

As previously discussed, the variation of density, ρ, with temperature and SOC is relevant not only to optimize the design, but also to accurately simulate the physical and chemical phenomena occurring during its operation. Density measurements were performed using an oscillating U-tube densimeter (Krüss Optronic DS7700) equipped with internal temperature control. Density was measured at each target SOC of interest (from 0% to 100%, at 10% intervals) for both electrolytes. Samples were prepared from the pure species and stored in 10 ml vessels. The color variation of the samples is shown in Fig. 2 (bottom). Additionally, temperature was varied between 10 °C and 40 °C, in 2 °C steps, covering the recommended safe operating range for VRFB (to avoid extreme positive and negative temperatures that could lead to species precipitation). The sample is injected into the densimeter with a syringe until the tubing is filled, and after reaching the desired temperature, the density value is directly obtained. Upon the end of each measurement and before introducing a new sample, the previous sample is drained, the device tubing is rinsed with deionized water, and it is further dried using the incorporated drying unit. To enhance accuracy, eight measurements (by both increasing and decreasing temperature) were performed to each sample for every temperature and SOC points considered.

3.3. Viscosity measurements

Vanadium electrolytes are Newtonian fluids and their viscosity plays a fundamental role in numerous physical processes such as mass transfer and pressure losses, significantly influencing the performance and efficiency of the VRFB. During battery operation, the viscosity of the electrolytes mainly varies due to the continuous changes in fluid SOC and temperature. The dynamic viscosity, μ, was measured using a Brookfield RVT rotational rheometer, featuring a spindle immersed in the test fluid that rotates at a controlled angular velocity. In response, the spindle experiences a viscous drag force opposing to its rotation. This force is measured by the device, providing an analog output in 0–100 scale. To convert this reading into actual dynamic viscosity values, the spindle must undergo a calibration procedure.

The original metallic spindles were unsuitable for electrolyte measurements due to its corrosive nature. Hence, it was necessary to design and manufacture a new spindle to meet two key requirements: chemical compatibility with the test fluids, and appropriate geometry to ensure readings within the viscometer measurement range. The spindle was designed based on the originals, but increasing the wetted surface area to enhance the force measurement sensitivity, and was machined in PVC. A comparison between the original metallic and the new plastic spindles with their relevant dimensions is provided in the

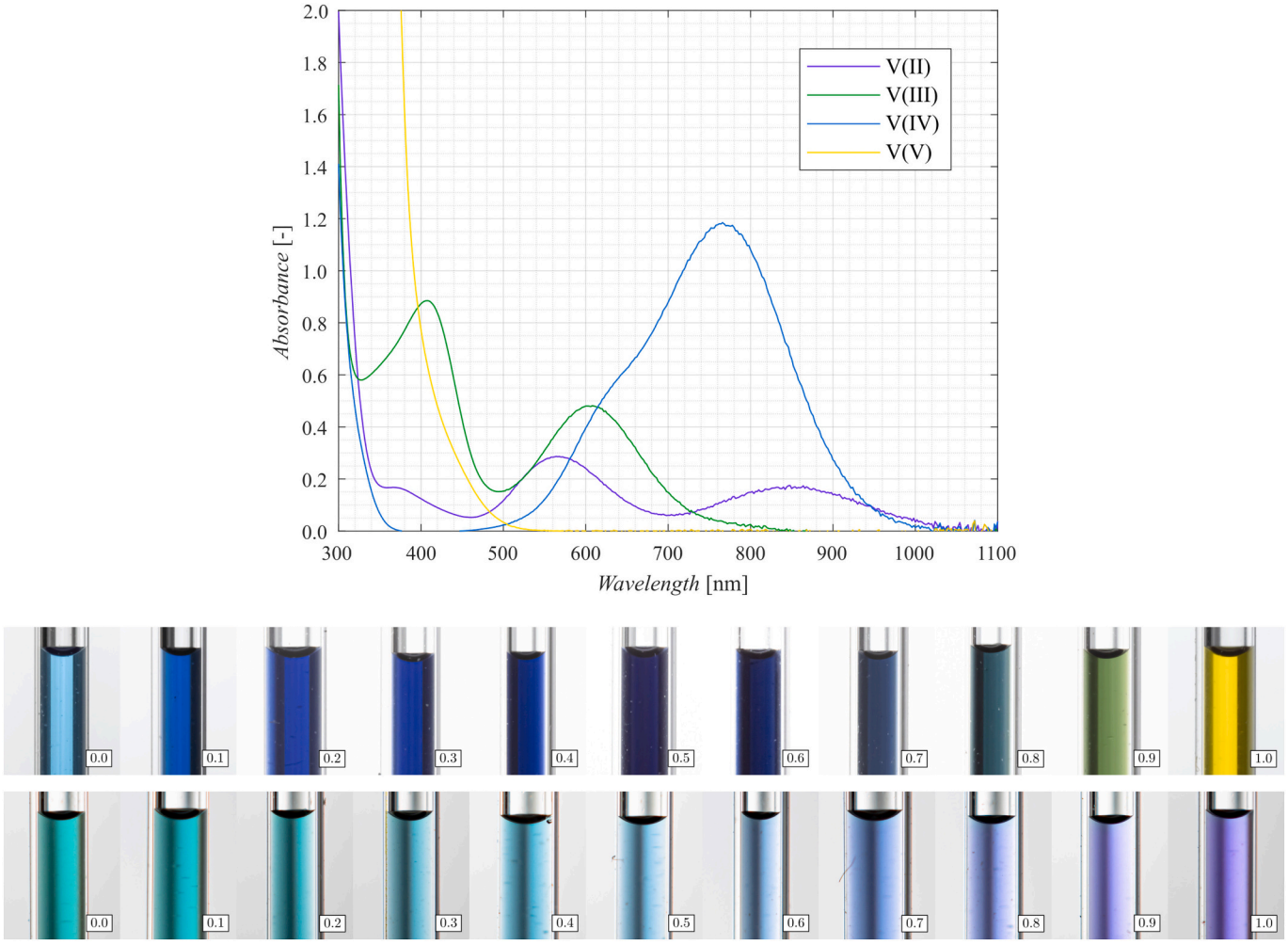

Fig. 2. Top: UV–Vis spectroscopy spectra obtained for the different vanadium species Bottom: Electrolyte color evolution at various SOC values. The upper row shows the posolyte, and the lower the negolyte samples, respectively.

Supplementary material (Fig. S1, Table S1). An average electrolyte viscosity value of 4.9 cP is commonly cited in the literature [21–23]. To calibrate the new spindle, test fluids with viscosities above and below the average value were prepared using glycerin-water mixtures, whose properties have been widely studied [24]. The actual viscosities of the calibration fluids were determined with an Engler-type rheometer, ranging from 0.95 cP to 8.86 cP. A linear correlation between the fluid viscosity and the rheometer reading with the new spindle was obtained. To carry out the electrolyte measurements, a beaker was filled with the test sample and immersed in a thermostatic water bath with controlled temperature. The Brookfield rheometer was positioned in a supporting arm that eased the immersion and extraction of the spindle into the fluid. The rotation speed was set to 100 rpm, to ensure an appropriate scale reading. For each sample, the dynamic viscosity was determined at six temperatures, namely 20 °C, 26 °C, 30 °C, 34 °C, 38 °C, and 42 °C. The reported value for each data point is the average of twelve experimental measurements, thereby enhancing the accuracy of the results.

3.4. Experimental facility

To assess the influence of the density and viscosity under actual VRFB operating conditions, an ad hoc test facility was designed and assembled. It consists of two 12-liter tanks, two magnetic-drive centrifugal pumps (Plastomec P051) mounting 120 W motors with frequency drive regulators, ancillary valves for independent flow control of each electrolyte and a 3 kW bidirectional power supply (Elektro-Automatik EA-PSB 10060-120 2U), featuring an in-house developed control software to manage the battery electrical operation. Furthermore, temperature (NTC thermistor, TDK) and flow rate (turbine flow meter, RS Pro) are measured in real-time for both the posolyte and the negolyte. All wetted parts, piping, and components are made from electrolyte-compatible materials such as PVC, PTFE or PVDF.

Fig. 3 shows the experimental facility and its piping and instrumentation diagram (P&ID). In addition to normal battery testing operation, the hydraulic system incorporates additional features as the equilibration of tank levels to compensate volume imbalances resulting from prolonged battery cycling tests. Fluid can also be pumped between reservoirs for electrolyte mixing and regeneration. For fluids analysis, sample extraction ports with needle valves are placed in each main pipeline to precisely control the extracted volume of electrolytes. In addition, the piping system can be easily drained when required. To establish an inert atmosphere inside the tanks and thereby preventing electrolyte degradation leading to a capacity loss, a nitrogen supply is available.

To enhance measurement precision, each flowmeter was calibrated independently, installed in situ, and tested across a range of flow rates spanning the expected operating conditions. Given the distinct working fluids for each device and the viscosity-sensitive nature of turbine flowmeters [25], the negative flowmeter was calibrated using V(II) and V(III) electrolytes at known temperatures, whereas for the positive flowmeter, V(IV) and V(V) solutions were used under similar conditions. The calibration constant obtained for each device was included in the

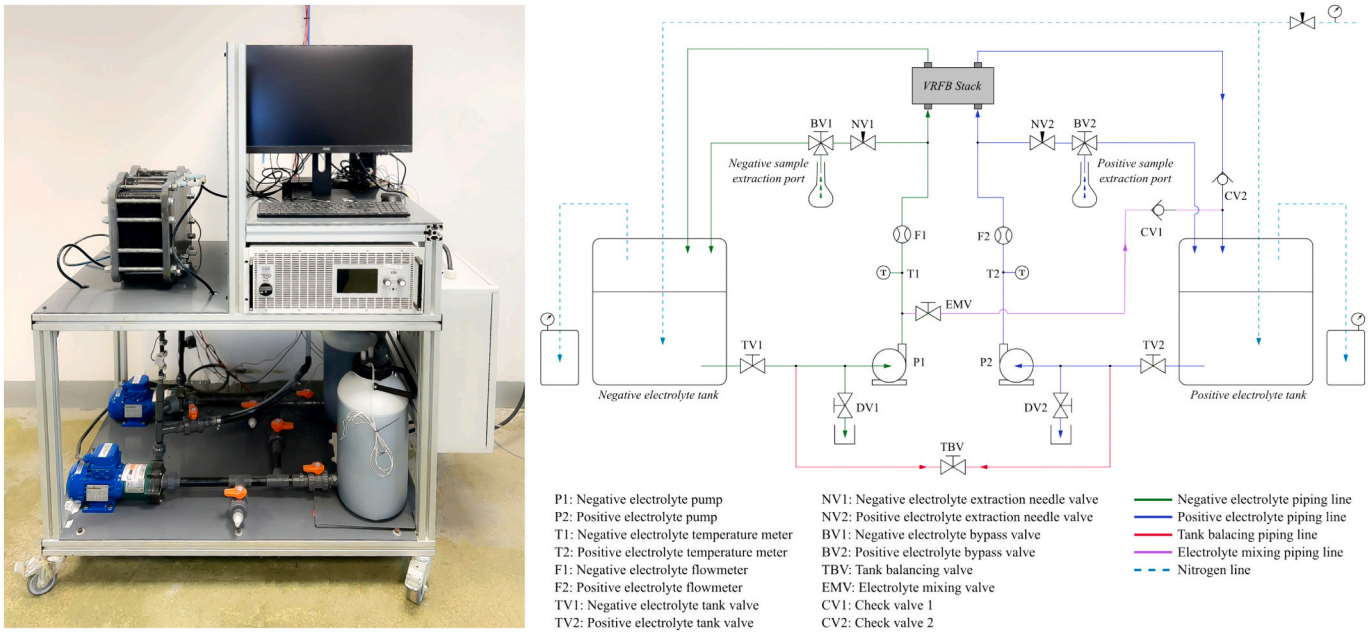

Fig. 3. Left: The manufactured experimental facility. Right: P&ID of the hydraulic system.

data acquisition code to enable individual correction during measuring. Furthermore, composition of the electrolytes at any given moment (and thus their SOC) was determined by UV–Vis spectroscopy.

3.5. VRFB experiments

One of the crucial parts of this work involved VRFB experiments, conducted in the test bench described in the previous section. Obtained results highlighted how sensitive the flow rate is to the operating temperature and physicochemical properties of the electrolytes. To perform these experiments, a five-cell 200 W stack with an electrode area of 240 cm^2 was employed. The volume of each electrolyte filling the stacks was approximately 3 l.

The procedure consisted of five charge-discharge cycles, starting and concluding with discharged electrolytes. Given the duration of the cycles, they were divided into two consecutive days. During charging, a current of 19.2 A (80 $mA{\cdot}cm^{-2}$) was applied until the stack voltage reached 8.25 V (1.65 $V{\cdot}cell^{-1}$). Subsequently, the stack voltage was maintained constant as the current decreased. The charging process concluded when the current was below 1.0 A (4.17 mA cm^{-2}). Similarly, during the discharge stages, 19.2 A were drawn from the VRFB as its voltage decreased until down to 3 V. Below this limit, the voltage was restricted, and the current decreased until reaching 1.0 A. At that point, discharge ceased. Before the first charge, between each half-cycle, and after the last discharge, an open-circuit interval of at least 1 min was established.

Regarding the flow rate regulation procedure, the values for negolyte and posolyte were adjusted at the beginning of the experiment to be roughly equal. Afterwards, the pumps remained unadjusted throughout the experiment, allowing flow rates to freely evolve as the electrolyte temperature and composition (SOC) varied. This approach was applied across four distinct flow rate levels. For each experiment, the pump operating frequencies, the approximate initial flow rates and the electrolyte pumping power are listed in Table 1. Prior to the experiments, the negative pump frequencies were set to values ranging from 60.0 to 40.0 Hz, whereas the positive ones were in the range 50.8 to 35.0 Hz.

The pump frequency selection was constrained by the Variable Frequency Drives (VFDs) maximum limit of 60 Hz and an operational minimum of 30.0 Hz to prevent flow instabilities and potential pump damage. Since the negolyte exhibits higher viscosity, its pump required higher frequencies to achieve equal flow rates, defining the tested range from 60 Hz down to 40 Hz, with intermediate frequencies of 53 Hz and 46 Hz chosen for uniform spacing. The positive pump frequencies were then determined experimentally to match the initial flow rates. The resulting flow rate values remained substantially higher than the stoichiometric minimum for all experiment levels, with initial flow factors [26] ranging from 25.6 to 12.5.

Table 1
Flow rate conditions in the VRFB experiments.

Experiment	Pump frequency [Hz]		Average initial flow rate [$l{\cdot}min^{-1}$]	Electrolyte pumping power [W]
	Positive	Negative		
1	50.8	60.0	0.90	0.82
2	45.6	53.0	0.77	0.70
3	39.7	46.0	0.60	0.55
4	35.0	40.0	0.44	0.40

Additionally, the pump power consumption was measured and found to be almost constant (approximately 50 W each). This constancy, likely resulting from the low operating flow rates, indicates that the instrumentation was not sensitive enough to detect variations in power consumption arising from changes in the fluids' physical properties.

Throughout the tests, the stack voltage and current, the temperature of both negolyte and posolyte and their flow rates were monitored in real-time at one-second interval. Furthermore, fluid samples were extracted regularly during both battery charging and discharging stages to determine their composition and SOC. This information enabled correlating the instantaneous physicochemical properties of the electrolytes and the circulating flow rate.

3.6. Hydraulic model

For a specific piping network, the total pressure drop of the pumping system can be estimated as a function of the flow rate. Conversely, pump manufacturers provide performance curves, typically using water, showing the head output of the device at different flow rates. Using these two expressions, the circulating flow rate and total pressure losses for a single operating condition can be determined.

The posolyte and negolyte piping networks of the experimental

facility were modeled independently. The total pressure drop for each network was attributed to four main contributions: elevation losses, friction losses, minor losses, and stack losses. Each contribution is discussed below.

Elevation losses: Represent the height difference between the free surface of the electrolyte in the tank and the discharge point of the piping system, located slightly above the electrolyte level. They can be estimated by:

$$\Delta P_{elevation} = \rho\, g \Delta z \tag{4}$$

where g represents the gravitational acceleration, and Δz is the height difference already mentioned.

Friction losses: They are determined using the well-known Darcy-Weisbach equation for straight pipe sections (Eq. (5)). In the experimental facility described in this work, multiple pipes with different lengths and inner diameters are involved. Therefore, to account for all friction losses, Eq. (5) can be written as a function of the electrolyte flow rate Q instead of its velocity u by:

$$\Delta P_{friction} = f \frac{L}{D} \frac{\rho\, u^2}{2} \tag{5}$$

$$\Delta P_{pipes} = \frac{8\, \rho\, Q^2}{\pi^2} \sum_{i=1}^{n_p} f_i \frac{L_i}{D_i^5} \tag{6}$$

where n_p represents the number of different pipes, f is the dimensionless Darcy friction factor, and L and D denote the length and inner diameter of the considered pipe. The pressure drop ΔP, fluid density and flow rate are expressed in SI units. The friction factor depends on the flow regime and roughness of the pipe. For laminar flow ($Re \leq 2300$), the value of f is calculated using the analytical expression 7. However, for turbulent flow ($Re > 2300$) the friction factor is typically obtained using empirical correlations or graphs. In the developed model, the Colebrook-White correlation (Eq. (8)) is employed, which requires iterative solving.

$$f = \frac{64}{Re} \tag{7}$$

$$\frac{1}{\sqrt{f}} = -2log_{10}\left(\frac{\varepsilon}{3.7D} + \frac{2.51}{Re\sqrt{f}}\right) \tag{8}$$

where ε is the absolute inner roughness of the pipe, and Re is the dimensionless Reynolds number, which can be calculated by:

$$Re = \frac{\rho\, u\, D}{\mu} = \frac{4\, \rho\, Q}{\pi\, \mu\, D} \tag{9}$$

Minor losses: Here, the pressure losses due to the flow circulating through valves, elbows, changes in pipe cross-section, fittings, and other components are included. The general expression to calculate the local pressure drop in a single piping component is given by Eq. (10). This expression can be modified to obtain Eq. (11), which quantifies the total pressure drop in the facility attributable to its fittings and components.

$$\Delta P_{local} = K \frac{\rho\, u^2}{2} \tag{10}$$

$$\Delta P_{minor} = \frac{8\, \rho\, Q^2}{\pi^2} \sum_{i=1}^{n_f} N_i \frac{K_i}{D_i^4} \tag{11}$$

where n_f represents the number of different accessories in the facility, N_i is the quantity of units for a considered element and K_i is the loss coefficient for fitting i, whose values are described and tabulated in the literature. Due to their complex geometry and features, turbine flow meters and check valves do not follow Eq. (10). The pressure loss in these elements is represented by Eq. (12), as specified by the manufacturers:

$$\Delta P_{flowmeter,check\ valve} = \left(\frac{Q}{c_1}\right)^{c_2} \tag{12}$$

where c_1 and c_2 are constants obtained from the datasheet curves. In this case, the flow rate must be expressed in $l{\cdot}min^{-1}$ and the pressure drop in bar, for both the flowmeters and check valves, respectively.

Stack losses: This group gathers contributions from the device inlet and outlet, manifolds, flow frame channels and electrodes. A significant part of the total pressure drop in stacks takes place at the electrodes, due to their morphology and porous nature [21,26,27]. The pressure loss in a porous medium is given by Darcy's law, which, for a rectangular electrode, can be expressed by:

$$\Delta P_{electrode} = \frac{\mu\, L_e\, Q}{\kappa\, t_e\, w_e\, N_{cells}} \tag{13}$$

where L_e, t_e, w_e are the electrode length, thickness and width after being compressed to enhance the electrochemical performance. N_{cells} is the number of cells of the stack, as the electrolyte flow rate Q is distributed among all cells, which are hydraulically connected in parallel. Finally, κ is the permeability of the electrode, expressed in m^2, which quantifies the resistance of the porous medium to fluid flow.

Given the battery dimensions and internal configuration, the model considers manifolds as equivalent straight pipes. Thus, the pressure losses across them are calculated using Eq. (5). The reactor inlet and outlet zones correspond to an abrupt cross-section expansion and contraction, respectively. Therefore, these losses are determined using the Eq. (10) with the loss coefficients defined by Eqs. (14) and (15) [28].

$$K_{stack\ inlet} = \left[1 - \left(\frac{d}{D}\right)^2\right]^2 \tag{14}$$

$$K_{stack\ outlet} = 0,42\left[1 - \left(\frac{d}{D}\right)^2\right] \tag{15}$$

where d and D represent the smaller and larger inner diameters in the sudden cross-section change, respectively.

Unlike other contributions, the pressure drop within the flow frame channels is difficult to determine via standard analytical correlations due to their complex internal geometries. Based on the authors' experimental characterization and supported by similar trends reported in the literature [29], these losses are significantly lower than those originating in the porous electrodes and follow a parabolic relationship with the flow rate. These losses are modeled using Eq. (16), with a dimensional head loss coefficient (K') of $31.5{\cdot}10^{12}$ $Pa{\cdot}(m^3{\cdot}s^{-1})^{-2}$. In summary, the total pressure losses for each electrolyte are calculated as the sum of contributions from elevation, friction, minor, flow meter, check valve (applicable to one circuit only) and stack losses.

$$\Delta P_{frame} = K' Q^2 \tag{16}$$

The pump output is incorporated into the model as a second-order polynomial with an appropriate fit. The curve provided by the manufacturer is given at 50 Hz. However, during the experiments, the flow-rate of the electrolytes was controlled by varying the pump frequency. Using dimensional analysis, it is possible to predict the head delivered by a pump at a variable impeller rotation speed by:

$$h_{pump} = m_0\left(\frac{\omega}{\omega_0}\right)^2 + m_1\left(\frac{\omega}{\omega_0}\right)Q + m_2 Q^2 \tag{17}$$

Here, ω_0 is the nominal frequency (50 Hz), ω is the operating frequency and m_0, m_1 and m_2 are the pump curve coefficients obtained at the mentioned nominal frequency.

The physical properties of the electrolytes are determined through the experimental measurements. Therefore, for given operating conditions (i.e., pump frequency, electrolyte temperature and SOC), the

developed model can estimate the circulating flow rate of each electrolyte independently, and decompose the various pressure drop contributions, thereby providing insight into the hydraulic resistance of each section of the piping network. The qualitative model structure is shown in Fig. 4.

4. Results

The detailed characterization of each electrolyte density and viscosity, along with their observed dependence on temperature and SOC, is paramount for a comprehensive understanding of the fluid dynamics performance of VRFBs. These physical properties directly govern the hydraulic behavior, affecting the total pressure losses. Accurate knowledge of these variations is essential for the precise modeling of flow rates and pressure drops, which are crucial for maintaining adequate electrolyte circulation and preventing mass transport limitations within the stack.

4.1. Density characterization

The visualization of density measurements for the positive and negative electrolytes, along with their corresponding contour plots, are presented in Fig. 5.

Both fluids exhibit values within a similar range, with density decreasing almost linearly as temperature increases, as stated in the literature [14]. However, it was found that the dependence of density on SOC differs between the negative and positive electrolytes. For a fixed temperature, the posolyte exhibits nearly constant density across the entire SOC range. On the contrary, for the negolyte the density decreases as the battery charges, as confirmed by the different slopes of the isodensity lines shown in the contour plots. At low SOC values, the negolyte exhibits a slightly higher density than the posolyte up to approximately SOC = 0.2. Beyond this point, the density gap between the two solutions widens with increasing SOC values.

The surfaces represented in Fig. 5 were fitted as functions of fluid temperature and SOC using polynomial equations, as described by:

$$\rho_k(SOC,T) = a_{00} + a_{10}\cdot SOC + a_{01}\cdot T + a_{11}\cdot SOC\cdot T + a_{20}\cdot SOC^2 + a_{02}\cdot T^2 \tag{18}$$

where ρ is expressed in g·cm^{-3}, T in °C, and SOC is dimensionless, ranging from 0 to 1. Subscript "k" denotes the electrolytes, with "n" standing for negative and "p" for positive. This notation will be maintained consistently throughout the whole text. The regression coefficients for the positive and negative electrolyte correlations are listed in Table 2.

While these differences may not be remarkable, they contribute to hydraulic variations, as density is proportional to pressure losses in pipes (Eq. (5)) and fittings (general minor losses, Eq. (10)), thereby influencing the actual electrolyte flow rate. Additionally, density also influences species diffusion and heat transfer processes [30].

4.2. Viscosity characterization

Maintaining the structure of the preceding section, the results of the dynamic viscosity measurements are presented in Fig. 6. During the experiments, the typical Arrhenius-exponential decrease of viscosity with increasing temperature was observed in all electrolyte samples. In general, the negative electrolyte exhibits higher viscosity values than the positive one. Regarding the SOC dependence, both fluids present a decreasing parabolic trend with increasing charge but the posolyte shows less dependence on this variable, with comparatively smaller variations than the negolyte. This is evident from the contour plots where, despite both fluids showing isoviscosity lines with a similar trend, their curvature is more pronounced for the negative electrolyte. The biggest viscosity gap between the two electrolytes occurs at SOC = 0, whereas as the charge increases the viscosity surfaces converge, yielding nearly equal values at SOC = 1.

Similar to the density analysis, the viscosity measurements were fitted with a polynomial using the SOC and electrolyte temperature as variables by:

$$\mu_k(SOC,T) = b_{00} + b_{10}\cdot SOC + b_{01}\cdot T + b_{11}\cdot SOC\cdot T + b_{20}\cdot SOC^2 + b_{02}\cdot T^2 \tag{19}$$

where μ is expressed in centipoise (cP), where 1 cP = 10^{-3} kg·m^{-1}·s^{-1}, T in °C, and SOC is dimensionless, ranging from 0 to 1. The regression coefficients for these equations are listed in Table 3.

In general, the dynamic viscosity of a fluid has a large influence on both laminar and turbulent pressure losses in pipes, since both are functions of the Reynolds number, with laminar losses being directly proportional to μ. Viscosity also impacts on the convective heat transfer (via the Prandtl number) and diffusion coefficients (via the Einstein-Stokes equation) [31].

The observed differences between our density and viscosity values and those reported by other authors can be primarily attributed to variations in electrolyte composition (vanadium and sulfate concentration, as well as additional additives). Our measurements show good agreement with the comprehensive study by Prieto-Díaz et al. [16], whose electrolyte composition falls within our studied range. Specifically, both studies report density values of approximately 1.35 g·cm^{-3} for the negative and positive electrolytes, with a greater influence of SOC variation observed for the negolyte. Furthermore, the characteristic trend of the negative electrolyte exhibiting a stronger SOC dependence for density and viscosity is consistent across both studies. Numerically, the results are highly similar, with deviation below 10%, confirming the general validity of our measurements despite minor compositional differences.

The influence of operational variables on viscosity trends is further supported by the work of Xiao et al. [32], who used a 1.5 M vanadium,

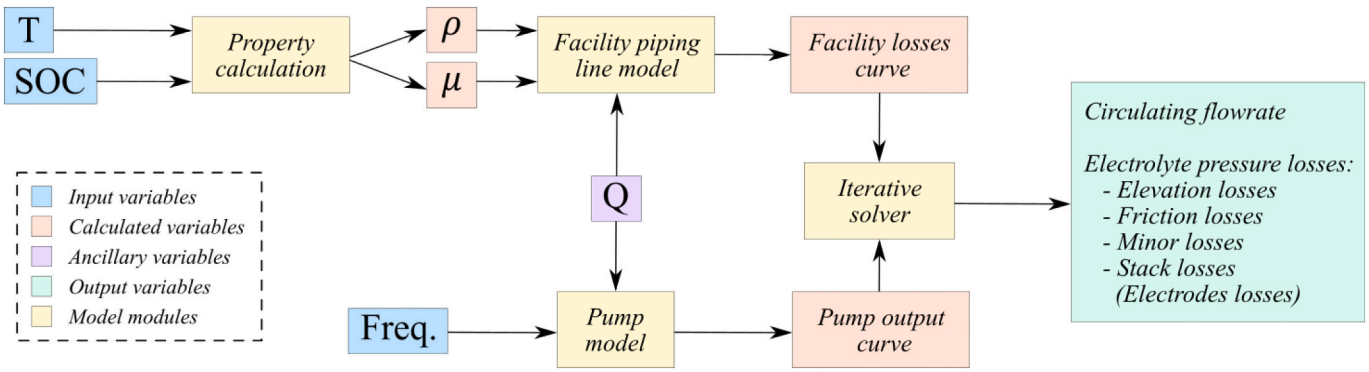

Fig. 4. Hydraulic model flowchart of the experimental facility.

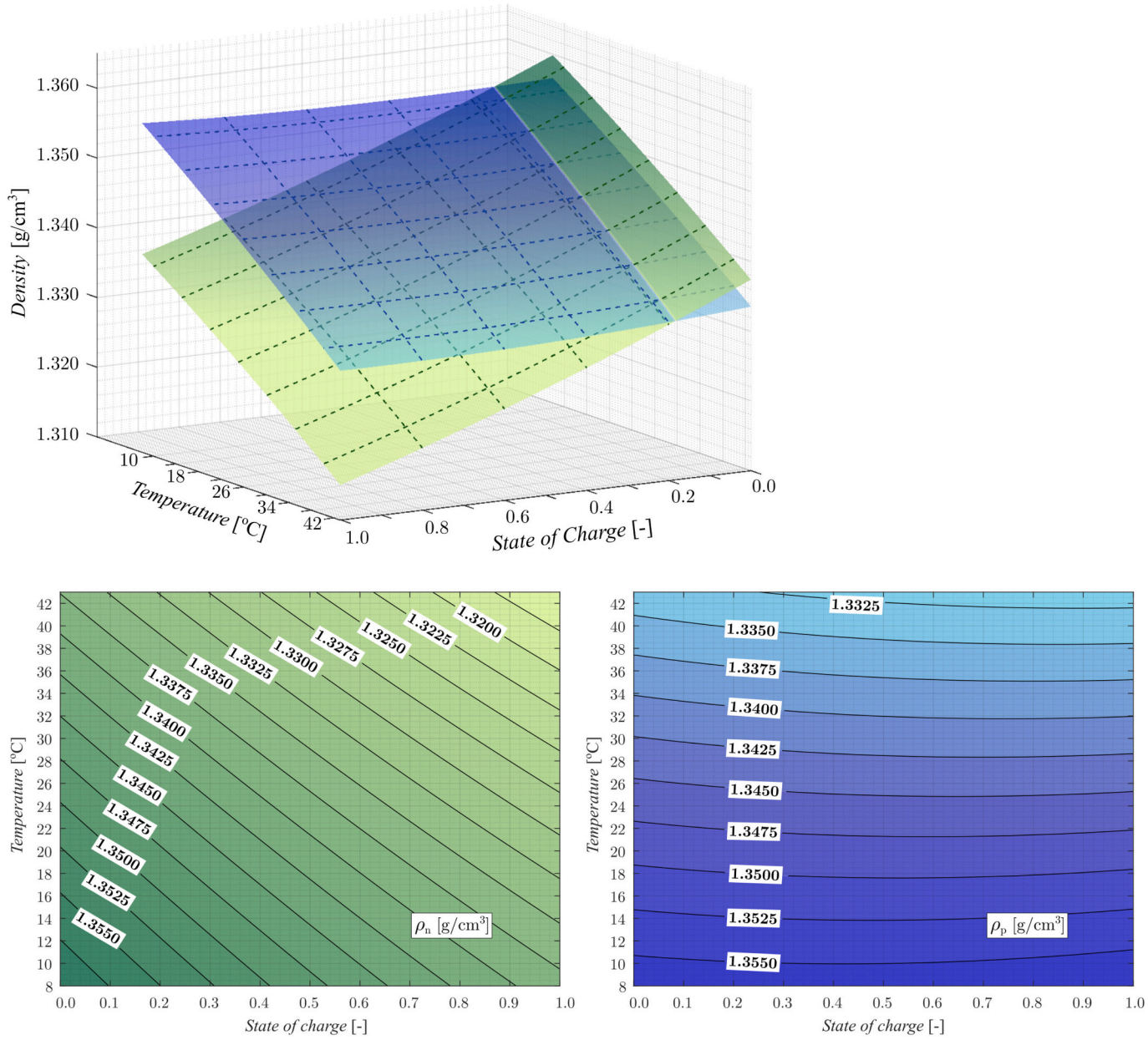

Fig. 5. Results of density measurements. The green surface represents the negative electrolyte, while the blue one corresponds to the positive electrolyte. (For interpretation of the references to color in this figure legend, the reader is referred to the web version of this article.)

Table 2
Regression coefficients for the electrolyte density correlations (Eq. (18)).

Coefficient	ρ_n	ρ_p	Unit	R^2
a_{00}	$1.364 \cdot 10^{0}$	$1.361 \cdot 10^{0}$	$g \cdot cm^{-3}$	$R_n^2 = 0.989$
a_{10}	$-2.489 \cdot 10^{-2}$	$-1.382 \cdot 10^{-3}$	$g \cdot cm^{-3}$	$R_p^2 = 0.988$
a_{01}	$-5.441 \cdot 10^{-4}$	$-5.687 \cdot 10^{-4}$	$g \cdot cm^{-3} \cdot °C^{-1}$	
a_{11}	$-2.620 \cdot 10^{-5}$	$-7.699 \cdot 10^{-5}$	$g \cdot cm^{-3} \cdot °C^{-1}$	
a_{20}	$3.614 \cdot 10^{-3}$	$2.557 \cdot 10^{-3}$	$g \cdot cm^{-3}$	
a_{02}	$-1.939 \cdot 10^{-6}$	$-1.794 \cdot 10^{-6}$	$g \cdot cm^{-3} \cdot °C^{-2}$	

3.875 M sulfates solution. Our measurements (Fig. 6) exhibit the same key behaviors reported in their study: for both electrolytes, viscosity decreases with increasing temperature, and the discharged state exhibits higher viscosity than the charged one. Notably, the negative electrolyte consistently shows a larger viscosity difference between the charged and discharged states compared to the positive electrolyte.

This variability is further corroborated by other studies, including those by Lawton et al. and Zhao et al. [33,34], which reported that viscosity and density increase with increasing sulfuric acid concentration. Similarly, Oriji et al. [35] demonstrated a quasi-exponential increase in the electrolyte viscosity as the sulfuric acid concentration rises. These findings highlight that even minor compositional deviations can lead to significant differences in physical properties, making rigorous direct numerical comparison across the different studies challenging.

Consequently, this discussion underscores the necessity of measuring the physical properties for the specific electrolyte composition used in this study and emphasizes the importance of the data presented.

4.3. VRFB experiments

Given the results from the physical properties, particularly the observed viscosity variation, a noticeable change in flow rates during the battery operation could be expected. The electrolyte flow rates

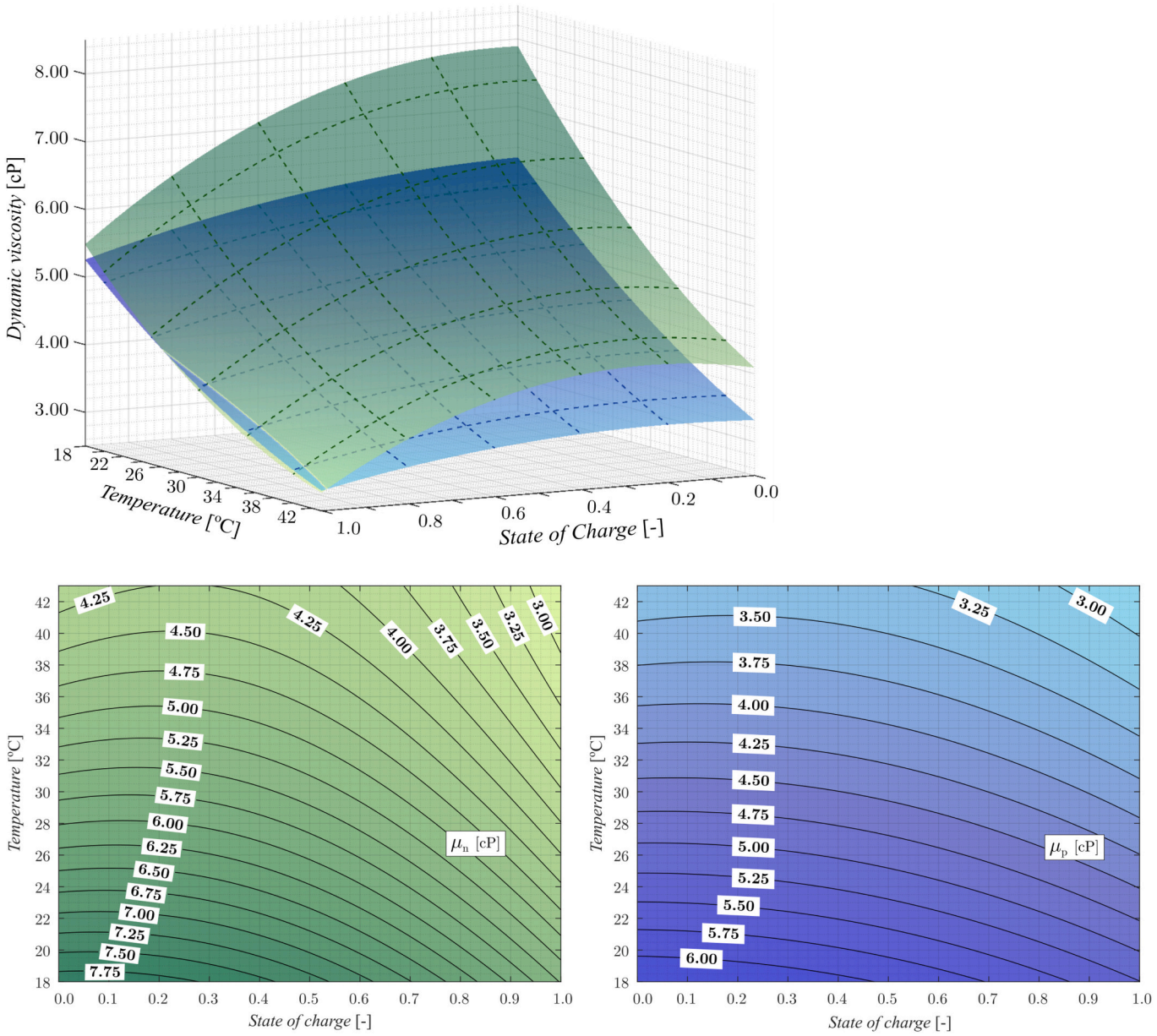

Fig. 6. Viscosity measurements results. Green surface: negative electrolyte, blue one: positive electrolyte. (For interpretation of the references to color in this figure legend, the reader is referred to the web version of this article.)

Table 3
Regression coefficients for the electrolyte viscosity correlations (Eq. (19)).

Coefficient	μ_n	μ_p	Unit	R^2
b_{00}	$1.261 \cdot 10^{1}$	$9.566 \cdot 10^{0}$	cP	$R_n^2 = 0.986$
b_{10}	$-5.372 \cdot 10^{-1}$	$-4.446 \cdot 10^{-1}$	cP	$R_p^2 = 0.992$
b_{01}	$-3.088 \cdot 10^{-1}$	$-2.124 \cdot 10^{-1}$	cP·°C^{-1}	
b_{11}	$4.312 \cdot 10^{-2}$	$1.873 \cdot 10^{-2}$	cP·°C^{-1}	
b_{20}	$-2.646 \cdot 10^{0}$	$-8.839 \cdot 10^{-1}$	cP	
b_{02}	$2.573 \cdot 10^{-3}$	$1.561 \cdot 10^{-3}$	cP·°C^{-2}	

monitored in the experiments described in Section 3.5 (Table 1) are plotted in Fig. 7 (left). Furthermore, the stack voltage recorded during Experiment 1 is shown together with the evolution of the flow rates in Fig. 7 (right). The time-flow rate, voltage and current profiles for Experiments 1 to 4 are provided in the Supplementary material (Figs. S2–S5).

The experimental results confirm that the electrolyte flow rate is a critical operational parameter. As shown in Table S3 (Supplementary material), a notable decrease in the total experiment duration was observed as circulating flow rates were progressively reduced, dropping from 17.57 h in Experiment 1 to 14.83 h in Experiment 4. This 15.6% reduction in operating time is primarily attributed to increased mass transport polarization at lower flow rates, which forces the system to reach the voltage cut-off limits earlier. Since the electrolyte flow rate governs the transport of active species to the electrode surface, an insufficient flow for a given current density leads to local reactant depletion. This not only results in poor electrochemical performance but also promotes secondary reactions, such as H_2/O_2 evolution, which can cause irreversible damage to stack components (e.g., bipolar plates and electrodes) through carbon oxidation and mechanical degradation. Consequently, the energy efficiencies significantly decreased as the flow rates were reduced (from 73.9% to 67.5% in the studied range). These efficiencies were calculated for each charge-discharge cycle according to Eq. (20):

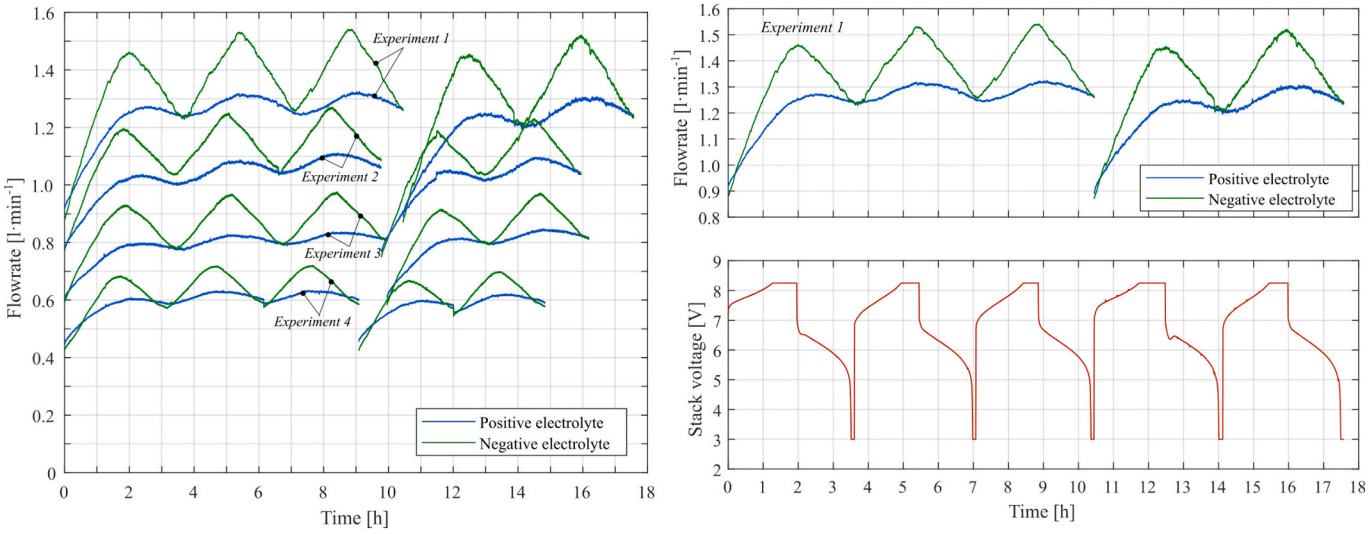

Fig. 7. Left: Electrolyte flow rates during the VRFB experiments. Right: Electrolyte Flow rates and battery potential during Experiment 1.

$$\eta_{energy} = \frac{\int_{t_{0,dis}}^{t_{f,dis}} \dot{W}\, dt}{\int_{t_{0,ch}}^{t_{f,ch}} \dot{W}\, dt} \tag{20}$$

where $\dot{W}$ represents the electric power, and t denotes time. Subscripts "0" and "f" refer to beginning and end of the test, while "dis" and "ch" indicate discharge and charge processes. Energy efficiencies for each cycle and tests are shown in Table 4. The decrease in average energy efficiency is noteworthy, becoming more pronounced with each successive experiment. Furthermore, the accumulated electric charge (capacity utilization) followed a similar trend (see Table S4 in Supplementary material). The charge capacity decreased from 158.4 A·h to 115.4 A·h, while the discharge capacity fell from 151.0 A·h to 111.4 A·h. These quantitative findings underscore that optimizing the flow rate is not merely a hydraulic concern but a fundamental requirement for maximizing the electrochemical energy density of the VRFB.

As illustrated in Fig. 7, each electrolyte presents different fluid dynamics behavior. Both exhibit an increase in flow rate during charging, reaching a local maximum at the end of the charge, followed by a decrease during discharge cycles, arriving at a local minimum when the discharge finishes. For each experiment, the electrolyte flow rates were initially set to be the same, and subsequently demonstrated a clear evolution during cycling, far from remaining constant, independently of the initial flow rate level. However, these flow rate differences are significantly more pronounced in the negolyte. This result agrees with observations from the viscosity characterization, where SOC variations induced greater viscosity changes in the negative electrolyte compared to the positive one. Table 5 gathers relevant values regarding these experiments, to quantitatively illustrate the non-negligible nature of these results.

Table 4
Energy efficiency of charge/discharge cycles.

Energy efficiency [%]						
	Cycle 1	Cycle 2	Cycle 3	Cycle 4	Cycle 5	Average
Experiment 1	72.0	75.6	75.9	71.0	75.1	73.9
Experiment 2	70.8	74.6	75.0	69.5	74.3	72.8
Experiment 3	66.6	73.0	73.2	67.0	72.6	70.5
Experiment 4	64.6	69.3	70.4	64.8	68.4	67.5

Table 5
Flow rate behavior of the electrolytes in VRFB experiments.

Test	Fluid	Initial flow rate [l·min^{-1}]	Max. flow rate [l·min^{-1}]	Temperature [°C]	Average charge-discharge flow rate difference [l·min^{-1}]
1	Posolyte	0.92	1.33	33.6	0.04
	Negolyte	0.88	1.54	33.1	0.25
2	Posolyte	0.77	1.11	33.0	0.04
	Negolyte	0.77	1.28	32.3	0.18
3	Posolyte	0.60	0.85	30.1	0.02
	Negolyte	0.59	0.98	29.2	0.15
4	Posolyte	0.45	0.63	28.0	0.02
	Negolyte	0.43	0.72	27.7	0.12

In addition to electrolytes composition evolution, temperature variation also influences fluid viscosity, and consequently their flow rates. Fig. 8 (left) shows the temperature profiles of the negolyte and the posolyte during Experiment 1, i.e., the experiment with the highest flow rates. As can be observed, the temperature increases notably during the initial charging cycle. From that point on, the temperature oscillates within a bounded range of around 4 °C for the rest of the experiment. In the discharging cycles, the electrolytes heat up, while their temperature decreases in the charging ones. This result can be expected, since the VRFB charging and discharging reactions are endothermic and exothermic, respectively [36,37].

To investigate the individual contributions of temperature and SOC to flow rate variation, a sensitive analysis was performed using a relative influence factor. A detailed description of the methodology and the results are provided in the Supplementary material. The analysis showed that the relative influence strongly depends on the operating point (T, SOC) and differs significantly between electrolytes. For both fluids, temperature has a dominant effect at low values ($T \leq 27$ °C). However, as temperature increases, the negative electrolyte exhibits significant regions where SOC predominates, whereas the positive electrolyte maintains temperature as the dominant factor across nearly its entire operational range.

To evaluate the contribution of the electric current to the temperature profile due to the Joule-Thomson effect, two additional experiments were performed, termed "Circulation tests 1 and 4". These experiments involved operating the pumps at the same frequencies of the previous Experiments 1 and 4 but without electrical operation of the battery, simultaneously monitoring the electrolyte temperature. The resulting profiles differ significantly to the temperature evolution in the charging-

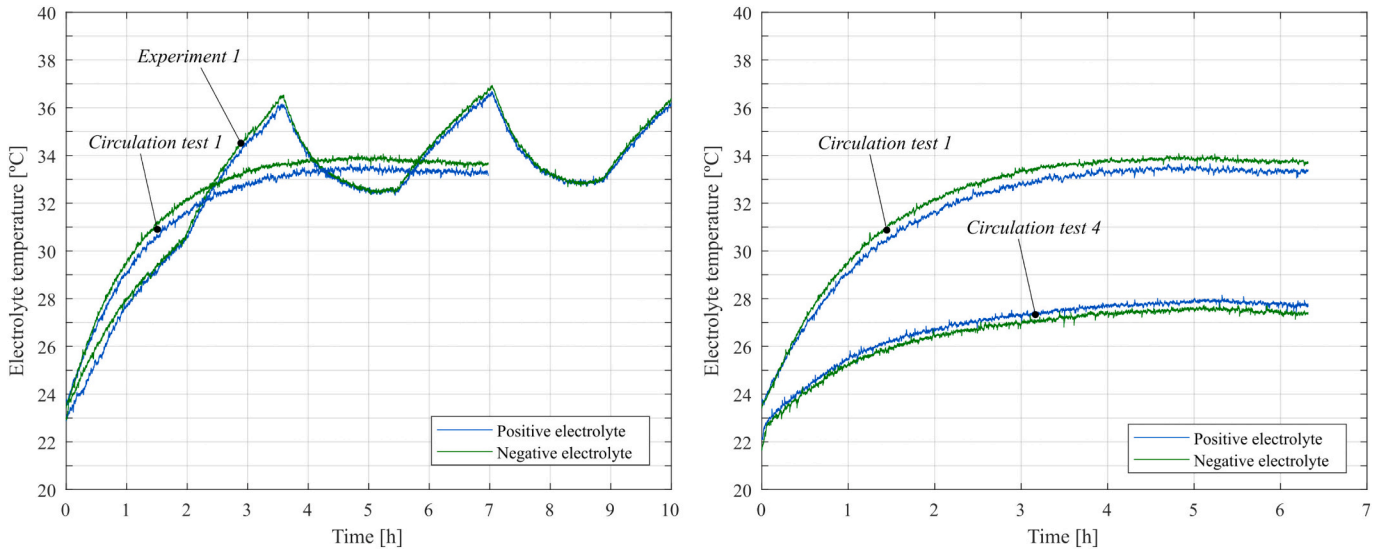

Fig. 8. Left: Electrolyte temperature evolution during Experiment 1 compared to Circulation test 1. Right: Electrolyte temperature profiles during Circulation tests 1 and 4.

discharging cycles. Circulation tests exhibit an asymptotic temperature growth until they reach a nearly constant value. When comparing the two Circulation tests, as depicted in Fig. 8 (right), there is a temperature gap of about 6 °C between the final values. The asymptotic temperature is higher in the experiment with greater flow rate, this being expected since the increase in the circulation rate leads to higher friction and consequently greater fluid heating.

During the initial charging phase, two opposing phenomena occur within the electrolyte. On the one hand, the fluid is initially heated as a result of its circulation through the hydraulic system and, besides, some heat is absorbed by the charging chemical reactions. A disparity exists between these contributions, as a portion of friction-generated heat is consumed by the reacting active species. As a result, the electrolyte temperature increases during this initial charge cycle, unlike what happens in the subsequent charging cycles where it decreases. However, the fluids heat up at a slower rate and exhibit lower temperatures than the observed in the circulation test as shown in Fig. 8 (left), which is noteworthy.

The observed dynamic evolution of electrolyte flow rates throughout charge and discharge cycles, fundamentally driven by the inherent dependence of electrolyte density and viscosity on both temperature and SOC, underscores the intricate hydraulic behavior within the VRFB. This complex interaction needs careful analysis of the electrochemical performance and provides a crucial foundation for understanding the system operational conditions.

4.4. Hydraulic model validation

Based on the insights of the electrolyte fluid dynamics, this section details the validation of the hydraulic model designed to predict and optimize these complex phenomena. The accurate prediction and control of the electrolyte flow are paramount for maximizing overall battery performance and global energy efficiency. Electrolyte flow rates below the optimal can critically limit the efficient transport of active species to the reaction sites and significantly contribute to parasitic energy consumption. Conversely, an optimized flow, estimated by a robust hydraulic model, ensures the efficient reactant delivery while minimizing ancillary power consumption, thereby enhancing the battery net energy output and overall operational stability.

Valuable information was obtained from the VRFB experiments (e.g., flow rates, electrolyte temperature and composition), and subsequently used to validate the computer code. Initially, it was assessed by using the average electrode permeability determined at the test facility, through a series of flow rate-differential pressure measurements between the stack inlet and outlet for each circuit independently. To obtain these permeability values, it was initially assumed that the pressure drop imposed by the electrodes constituted the major contribution in the stack, neglecting the other ones like flow frames and manifolds. This assumption seems reasonable, as the relationship between the measured pressure differences and flow rates was virtually linear, corroborating the minor influence of the other pressure drop sources, since they all scale quadratically with this variable. However, the permeability values were further recalculated through an iterative process to improve the accuracy of the computational model.

The average permeability obtained for the positive and negative electrolytes were $\kappa_p = 7.25{\cdot}10^{-11}$ m^2 and $\kappa_n = 6.96{\cdot}10^{-11}$ m^2, respectively. These values and all other relevant geometric data of the test facility were introduced into the model, which was computed for the experimental points listed in Table S2 of the Supplementary material. To evaluate how well the flow rate of both posolyte and negolyte estimated by the model fits the experimental data, root mean squared error (Q_{RMSE}) was calculated as:

$$Q_{RMSEk} = \sqrt{\frac{1}{n}\sum_{i=1}^{n}\left(Q_{model,i} - Q_{experiment,i}\right)^2} \tag{21}$$

where subscript k means posolyte (p) or negolyte (n). Using this model configuration, $Q_{RMSE,p} = 2.81{\cdot}10^{-2}$ l·min^{-1} and $Q_{RMSE,n} = 8.78{\cdot}10^{-2}$ l·min^{-1} were obtained. The flow rate values calculated by this model and the absolute value of the relative error of each data point are shown in Fig. 9, labeled as “Approach 1”. As expected, and in good agreement with existing literature, a significant percentage of pressure losses occurs within the porous electrodes, according to the model. For the experimental data considered, this analysis indicates that an average of 90.6% and 90.3% of the total pressure losses in the positive and negative circuits, respectively, occur in the stack, while the electrodes account for 73.0% and 74.6% of the stack positive and negative pressure drop, respectively.

To evaluate the achievable precision of the low-cost computational model, the permeability values that minimize the root mean square error of the flow rate (Q_{RMSE}) were determined. These results were labeled as “Approach 2” and compared with the original estimates. The optimization was performed independently for the positive and negative sides using an exhaustive search technique over a bounded range (from

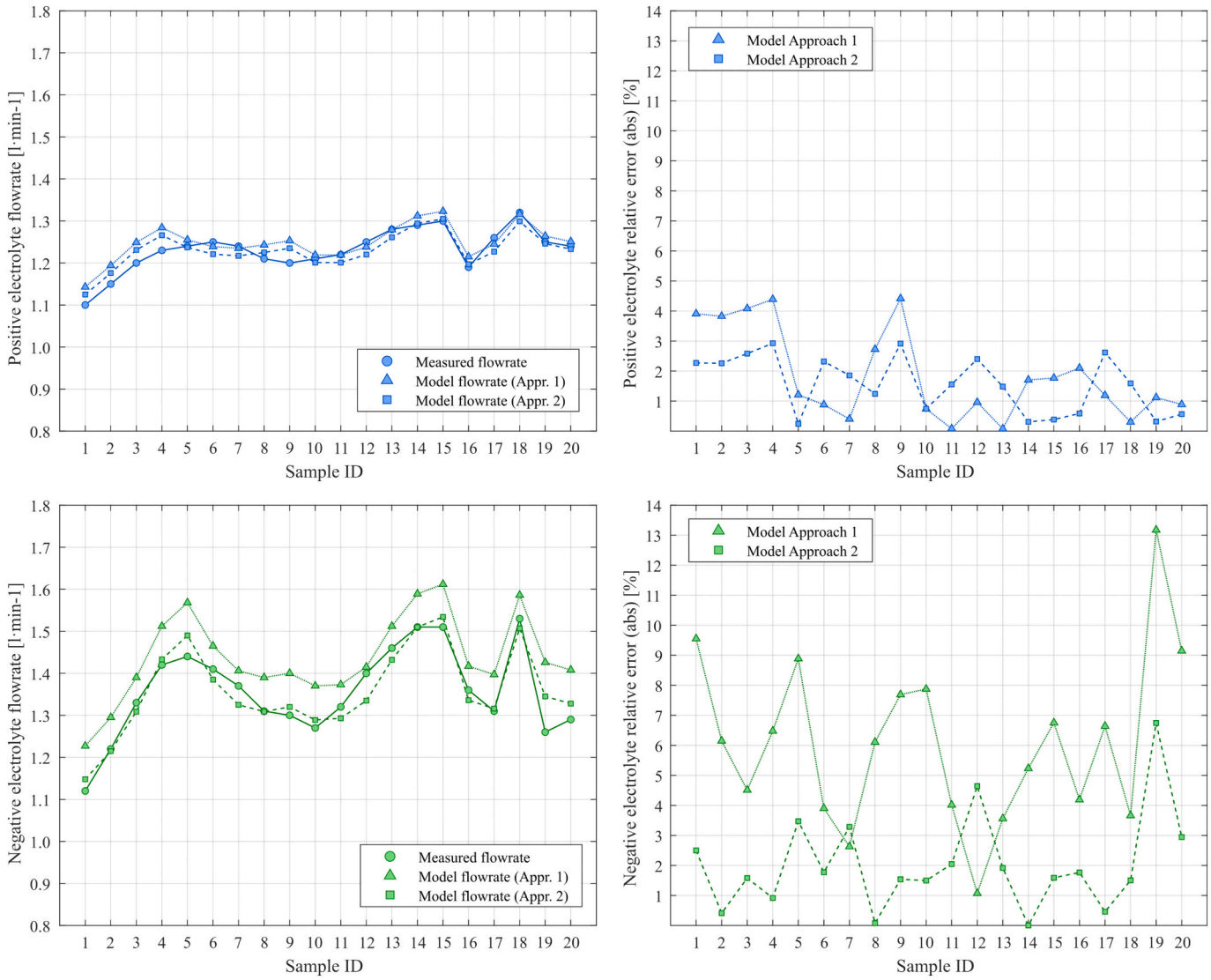

Fig. 9. Results obtained from numerical simulations of the hydraulic model. The top panel displays the measured vs. calculated flow rate (left) and the absolute relative error (right) for the positive electrolyte. The bottom panel presents the corresponding flow rate and absolute relative error for the negative electrolyte.

$6{\cdot}10^{-11}$ m^2 to $1{\cdot}10^{-10}$ m^2) with a fixed permeability increment of $1{\cdot}10^{-13}$ m^2 per iteration. The search terminated upon reaching the upper limit of the range. The optimized permeability values were then selected as those yielding the minimum global Q_{RMSE}. This procedure produced new permeability values $\kappa_p' = 7.05{\cdot}10^{-11}$ and $\kappa_n' = 6.27{\cdot}10^{-11}$ m^2 for the positive and negative sides, respectively.

With these new permeability values, *Approach 2* significantly improved the model's agreement with experimental data, particularly for the negative circuit, as demonstrated by Q_{RMSE} values of $2.21{\cdot}10^{-2}$ $l{\cdot}min^{-1}$ and $3.42{\cdot}10^{-2}$ $l{\cdot}min^{-1}$ for the posolyte and negolyte, respectively. In this simulation, the average stack pressure losses accounted for 90.5% and 91.3% of the total losses in the positive and negative circuits, respectively, with 74.0% and 77.3% of the stack head losses attributable to the porous electrodes. The numerical values and errors obtained in this new calculation are presented in Fig. 9, alongside the results from the initial approach.

Although an exhaustive characterization of the electrolyte density and viscosity was previously performed, only a few parameters are required as inputs to estimate the actual flow rate of each electrolyte due to the simplicity of this model. Consequently, the error in the calculated values by the model relative to the measured data remains within a reasonable limit as expected. Even when the obtained results are very accurate, the current model has certain limitations that need to be further improved such as the actual pressure drops imposed by the flowmeters when measuring electrolytes and by the complex flow frame geometry. Despite these uncertainties, the model yielded relative errors below 5% with a very low computational cost.

The main sources of error inherent to the model are, primarily: (i) uncertainties in the experimental measurements used to determine the physical properties, which propagates directly to the model; (ii) the assumption of constant electrode permeability, which translates the uncertainty in the calibrated permeability value into flow rate uncertainty; and (iii) the reliance on the manufacturer's pump curve, whereby the associated uncertainty introduces a direct error in the predicted flow rate.

Additional sources of error, such as pressure drop in pipes and fittings, sensor readings, or the geometrical simplifications of the stack channels, have only a minor impact on the flow rate calculation. Furthermore, vanadium migration across the membranes (crossover) is an inherent phenomenon in VRFBs, leading to concentration changes in the electrolyte and, consequently, variations in their physical properties. However, Noriega et al. [38] reported that crossover induces less than 0.6% change in volume per day in long duration experiments (several days). In our study, these effects are considered negligible and do not

significantly affect the accuracy of the model.

Given these uncertainties and the simplifications, the model performance with respect to the operational variables has been analyzed. For the experimental points considered, the model accuracy is not systematically correlated with the values of the measured parameters. This indicates that prediction errors are primarily influenced by stochastic uncertainties in the input parameters or by the model simplifications (systemic and calibration errors), rather than by the temperature and SOC themselves.

The comprehensive characterization of electrolyte density and viscosity presented in this study, together with the computational model, provide crucial insights into the dynamic behavior of VRFB hydraulic systems. These findings are pivotal for optimizing the hydraulic system, as they enable precise modeling of flow rates and pressure losses as a function of the SOC and temperature. Optimizing pump operation based on the variation of the physical properties offers a significant way for reducing parasitic energy losses, thereby enhancing the overall electrochemical energy efficiency of the battery. This understanding allows the development of more sophisticated control strategies for the dynamic adjust of the pump settings to maintain the optimal flow of electrolyte, ensuring the efficient transport of active species while minimizing the power consumption.

5. Conclusions

An experimental study was performed for to characterize in depth the density and viscosity of vanadium electrolytes across the full SOC range (from 0 to 1) and the safe operating temperature range (10 °C to 40 °C). The measurements revealed distinct behaviors for the two electrolytes: the negative electrolyte (negolyte) showed a stronger dependence on SOC changes, particularly in terms of viscosity, compared to the positive electrolyte (posolyte).

Accurate empirical expressions for density and viscosity as a function of SOC and temperature were derived, providing essential inputs for modeling. Experiments using a 5-cell VRFB stack demonstrated that variations in these physical properties produced different flow rate responses for each electrolyte during charge-discharge cycles, with flow rates increasing during charging (local maximum) and decreasing during discharging (local minimum). Importantly, hydraulic conditions had a significant impact on energy performance: progressively lower circulating flow rates resulted in shorter overall experiment durations and reduced the average overall efficiency from 73.9% to 67.5%.

A low-cost numerical model was successfully developed to estimate the electrolyte flow rates under given operating conditions, achieving relative errors below 5% compared to experimental measurements. The model demonstrated that accounting for the evolving physical properties of the electrolytes is essential for accurate flow rate predictions. Using the model, it was quantified that approximately 90% of the total pressure losses occur within the stack, with the electrodes contributing more than 70% of those losses, highlighting the key target for hydraulic optimization. Furthermore, a sensitivity analysis showed that the relative influence of temperature versus SOC on flow rate variations strongly depends on the operating point and the electrolyte type: the negolyte is primarily temperature-governed by at low temperature but becomes SOC-dominated at higher temperature, whereas the posolyte remains largely temperature-dominated across nearly the entire operational range.

These results validate the hydraulic model, which, together with the mathematical correlations for the electrolyte physical properties, constitutes a powerful predictive tool suitable for direct integration into the Battery Management System (BMS) of practical devices. This work enables a novel approach to VRFB control, shifting from traditional current-based methods to real-time predictive control grounded on the actual physical state of the electrolyte (temperature and SOC). Such an approach facilitates the dynamic optimization of pumping power, ensuring that the circulating flow rate always exceeds the minimum required stoichiometric flow while minimizing the consumption of ancillary system and maximizing energy efficiency.

CRediT authorship contribution statement

Álvaro Ibáñez: Writing – original draft, Visualization, Investigation, Formal analysis. **Manuel Montiel:** Writing – review & editing, Supervision, Methodology, Funding acquisition, Conceptualization. **Andrés Tejero:** Investigation, Formal analysis. **Ignacio Ortiz de Landazuri:** Validation, Formal analysis. **Antonio Lozano:** Writing – review & editing, Validation. **Jorge Barroso:** Supervision, Conceptualization. **Félix Barreras:** Writing – review & editing, Methodology, Funding acquisition.

Declaration of competing interest

The authors declare that they have no known competing financial interests or personal relationships that could have appeared to influence the work reported in this paper.

Acknowledgements

The authors acknowledge the support and work of Ana Quílez and Iván Manrique during the hydraulic facility assembly and experiments. This research has been developed within the CSIC Interdisciplinary Thematic Platform (PTI+) Transición Energética Sostenible+ (PTI-TRANSENER+) as part of the CSIC program for the Spanish Recovery, Transformation and Resilience Plan funded by the Recovery and Resilience Facility of the European Union, established by the Regulation (EU) 2020/2094. The authors would like also to acknowledge the financial support provided by the Spanish Ministry of Science, Innovation and Universities under projects MAFALDA (ref.: PID2021-126001OB-C32) and DECODER (ref.: PID2024-158394OB-C21), and to the Aragon Government, Spain, under the projects T06_23R and FLUFEE (PROY_T53_24).

Appendix A. Supplementary data

Supplementary data to this article can be found online at https://doi.org/10.1016/j.est.2026.120760.

Data availability

Data available at Mendeley Data (DOI: 10.17632/fgz5md6dzs)
Influence of the physical properties of electrolytes on the behavior of all-vanadium redox flow batteries (Original data) (Mendeley Data)

References

[1] Red Eléctrica Española, Spanish Electric Grid - Evolution of renewable and not renewable energy generation, 2025. https://www.ree.es/es/datos/generacion. (Accessed 27 March 2025).
[2] W. Gorman, A. Mills, M. Bolinger, R. Wiser, N.G. Singhal, E. Ela, et al., Motivations and options for deploying hybrid generator-plus-battery projects within the bulk power system, Electr. J. 33 (2020) 106739, https://doi.org/10.1016/j.tej.2020.106739.
[3] M. Faisal, M.A. Hannan, P.J. Ker, A. Hussain, M. Bin Mansor, F. Blaabjerg, Review of energy storage system technologies in microgrid applications: Issues and challenges, IEEE Access 6 (2018) 35143–35164, https://doi.org/10.1109/ACCESS.2018.2841407.
[4] L. Trahey, F.R. Brushett, N.P. Balsara, G. Ceder, L. Cheng, Y.M. Chiang, et al., Energy storage emerging: a perspective from the Joint Center for Energy Storage Research, Proc. Natl. Acad. Sci. U. S. A. 117 (2020) 12550–12557, https://doi.org/10.1073/pnas.1821672117.
[5] M. Skyllas-Kazacos, M. Rychcik, R.G. Robins, A.G. Fane, M.A. Green, New all-vanadium redox flow cell, J. Electrochem. Soc. (1986) 1057–1058.
[6] M. Skyllas-Kazacos, Secondary batteries – flow systems | Vanadium Redox-Flow Batteries, in: Encycl. Electrochem. Power Sources, Elsevier, 2009, pp. 444–453, https://doi.org/10.1016/B978-044452745-5.00177-5.

[7] T. Shibata, T. Kumamoto, Y. Nagaoka, K. Kawase, K. Yano, Redox flow battery system for the stable supply of renewable energy, IEEE Electr. Insul. Mag. 30 (2014) 48–50, https://doi.org/10.1109/MEI.2014.6943434.
[8] C. Roth, J. Noack, M. Skyllas-Kazacos, Flow Batteries: From Fundamentals to Applications, John Wiley & Sons, 2022.
[9] M. Skyllas-Kazacos, M.H. Chakrabarti, S.A. Hajimolana, F.S. Mjalli, M. Saleem, Progress in flow battery research and development, J. Electrochem. Soc. 158 (2011) R55, https://doi.org/10.1149/1.3599565.
[10] P.A. Prieto-Díaz, S.E. Ibáñez, M. Vera, Fluid dynamics of mixing in the tanks of small vanadium redox flow batteries: Insights from order-of-magnitude estimates and transient two-dimensional simulations, Int. J. Heat Mass Transf. 216 (2023) 124567, https://doi.org/10.1016/j.ijheatmasstransfer.2023.124567.
[11] A. Mousa, Chemical and Electrochemical studies ofV (III) and V (II) Solutions in Sulfuric Acid Solution for Vanadium Battery Applications, PhD Thesis,, Univ New South Wales, Aust 2003.
[12] F. Rahman, M. Skyllas-Kazacos, Vanadium redox battery: positive half-cell electrolyte studies, J. Power Sources 189 (2009) 1212–1219, https://doi.org/10.1016/j.jpowsour.2008.12.113.
[13] W.G. Xu, Y. Qin, F. Gao, J.G. Liu, C.W. Yan, J.Z. Yang, Determination of volume properties of aqueous vanadyl sulfate at 283.15 to 323.15 K, Ind. Eng. Chem. Res. 53 (2014) 7217–7223, https://doi.org/10.1021/ie402040h.
[14] S. Ressel, F. Bill, L. Holtz, N. Janshen, A. Chica, T. Flower, et al., State of charge monitoring of vanadium redox flow batteries using half cell potentials and electrolyte density, J. Power Sources 378 (2018) 776–783, https://doi.org/10.1016/j.jpowsour.2018.01.006.
[15] M. Skyllas-Kazacos, L. Cao, M. Kazacos, N. Kausar, A. Mousa, Vanadium electrolyte studies for the vanadium redox battery-a review, ChemSusChem 9 (2016) 1521–1543, https://doi.org/10.1002/cssc.201600102.
[16] P.A. Prieto-Díaz, A.A. Maurice, M. Vera, Measuring density and viscosity of vanadium electrolytes: A database with multivariate polynomial fits, J. Energy Storage 94 (2024) 112429, https://doi.org/10.1016/j.est.2024.112429.
[17] Q. Xu, T.S. Zhao, C. Zhang, Effects of SOC-dependent electrolyte viscosity on performance of vanadium redox flow batteries, Appl. Energy 130 (2014) 139–147, https://doi.org/10.1016/j.apenergy.2014.05.034.
[18] K.W. Knehr, E. Agar, C.R. Dennison, A.R. Kalidindi, E.C. Kumbur, A transient vanadium flow battery model incorporating vanadium crossover and water transport through the membrane, J. Electrochem. Soc. 159 (2012) A1446–A1459, https://doi.org/10.1149/2.017209jes.
[19] X. Li, J. Xiong, A. Tang, Y. Qin, J. Liu, C. Yan, Investigation of the use of electrolyte viscosity for online state-of-charge monitoring design in vanadium redox flow battery, Appl. Energy 211 (2018) 1050–1059, https://doi.org/10.1016/j.apenergy.2017.12.009.
[20] R.P. Brooker, C.J. Bell, L.J. Bonville, H.R. Kunz, J.M. Fenton, Determining vanadium concentrations using the UV-Vis response method, J. Electrochem. Soc. 162 (2015) A608–A613, https://doi.org/10.1149/2.0371504jes.
[21] A. Tang, J. Bao, M. Skyllas-Kazacos, Studies on pressure losses and flow rate optimization in vanadium redox flow battery, J. Power Sources 248 (2014) 154–162, https://doi.org/10.1016/j.jpowsour.2013.09.071.
[22] X. Ma, H. Zhang, F. Xing, A three-dimensional model for negative half cell of the vanadium redox flow battery, Electrochim. Acta 58 (2011) 238–246, https://doi.org/10.1016/j.electacta.2011.09.042.
[23] Z. Wei, J. Zhao, M. Skyllas-Kazacos, B. Xiong, Dynamic thermal-hydraulic modeling and stack flow pattern analysis for all-vanadium redox flow battery, J. Power Sources 260 (2014) 89–99, https://doi.org/10.1016/j.jpowsour.2014.02.108.
[24] N. Cheng, Formula for the viscosity of a glycerol-water mixture, Ind. Eng. Chem. Res. 47 (2008) 3285–3288, https://doi.org/10.1021/ie071349z.
[25] S. Guo, L. Sun, T. Zhang, W. Yang, Z. Yang, Analysis of viscosity effect on turbine flowmeter performance based on experiments and CFD simulations, Flow Meas. Instrum. 34 (2013) 42–52, https://doi.org/10.1016/j.flowmeasinst.2013.07.016.
[26] A. Trovò, F. Picano, M. Guarnieri, Comparison of energy losses in a 9 kW vanadium redox flow battery, J. Power Sources 440 (2019), https://doi.org/10.1016/j.jpowsour.2019.227144.
[27] Y. Cao, P. Li, J. Zhou, Z. Sui, X. Zhou, Pressure drop and residence time distribution in carbon-nanofiber/graphite- felt composite for single liquid-phase flow, Ind. Eng. Chem. Res. 50 (2011) 9431–9436, https://doi.org/10.1021/ie2004187.
[28] F.M. White, Fluid Mechanics 8th edition, vol. 11, McGraw Hill, 2017.
[29] S. Pawloski, J.G. Crespo, S. Velizarov, Pressure drop in reverse electrodialysis: Experimental and modeling studies for stacks with variable number of cell pairs, J. Membr. Sci. 462 (2014) 96–111, https://doi.org/10.1016/j.memsci.2014.03.020.
[30] R.B. Bird, W.E. Stewart, Lightfoot, Transport phenomena, John Wiley & Sons, 1960.
[31] J.R. Welty, C.E. Wicks, R.E. Wilson, G.L. Rorrer, Fundamentals of Momentum, Heat and Mass Transfer, 6th edition, John Wiley & Sons, 2014.
[32] S. Xiao, L. Yu, L. Wu, L. Liu, X. Qiu, J. Xi, Broad temperature adaptability of vanadium redox flow battery-Part 1: Electrolyte research, Electrochim. Acta 187 (2016) 525–534, https://doi.org/10.1016/j.electacta.2015.11.062.
[33] J. Lawton, S. Tiano, D. Donnelly, S. Flanagan, T. Arruda, The effect of sulfuric acid concentration on the physical and electrochemical properties of vanadyl solutions, Batteries 4 (2018) 40, https://doi.org/10.3390/batteries4030040.
[34] Y. Zhao, L. Liu, X. Qiu, J. Xi, Revealing sulfuric acid concentration impact on comprehensive performance of vanadium electrolytes and flow batteries, Electrochim. Acta 303 (2019) 21–31, https://doi.org/10.1016/j.electacta.2019.02.062.
[35] G. Oriji, Y. Katayama, T. Miura, Investigation on V(IV)/V(V) species in a vanadium redox flow battery, Electrochim. Acta 49 (2004) 3091–3095, https://doi.org/10.1016/j.electacta.2004.02.020.
[36] C. Blanc, A. Rufer, Understanding the Vanadium Redox Flow Batteries, in: Paths to Sustain. Energy, InTech, 2010, https://doi.org/10.5772/13338.
[37] D. Bryans, V. Amstutz, H.H. Girault, L.E.A. Berlouis, Characterisation of a 200 kW/400 kWh Vanadium Redox Flow Battery, Batteries 4 (2018) 54, https://doi.org/10.3390/batteries4040054.
[38] S. Oreiro, A. Bentien, J. Sloth, M. Rahimi, M. Madsen, T. Drechsler, Crossover analysis in a commercial 6 kW/43kAh vanadium redox flow battery utilizing anion exchange membrane, Chem. Eng. J. 490 (2024) 151947, https://doi.org/10.1016/j.cej.2024.151947.